

## Origin of perpendicular magnetic anisotropy in $\text{Co}_x\text{Fe}_{3-x}\text{O}_{4+\delta}$ thin films studied by x-ray magnetic circular and linear dichroisms

Jun Okabayashi <sup>1</sup>, Masaaki A. Tanaka <sup>2</sup>, Masaya Morishita,<sup>2</sup> Hideto Yanagihara <sup>3</sup>, and Ko Mibu <sup>2</sup>

<sup>1</sup>*Research Center for Spectrochemistry, The University of Tokyo, Bunkyo-ku, Tokyo 113-0033, Japan*

<sup>2</sup>*Graduate School of Engineering, Nagoya Institute of Technology, Nagoya 466-8555, Japan*

<sup>3</sup>*Department of Applied Physics, University of Tsukuba, Tsukuba 305-8573, Japan*



(Received 15 January 2022; revised 19 March 2022; accepted 28 March 2022; published 14 April 2022)

We investigate the element-specific spin and orbital states and their roles in magnetic anisotropy in Co-ferrite [ $\text{Co}_x\text{Fe}_{3-x}\text{O}_{4+\delta}$  (001)] thin films which exhibit perpendicular magnetic anisotropy (PMA). The origin of PMA in the low- $x$  region ( $x < 1$ ) can be mainly explained by the large perpendicular orbital magnetic moments in the  $\text{Co}^{2+}$  ( $3d^7$ ) states detected by x-ray magnetic circular dichroism and x-ray magnetic linear dichroism (XMLD). The XMLD for a PMA film ( $x = 0.2$ ) with a square hysteresis curve shows the oblate charge distribution in the  $\text{Co}^{2+}$  site, which is consistent with the change in local nearest-neighbor distance in Co detected by extended x-ray absorption fine structure analysis. Our finding reveals that the microscopic origin of PMA in Co ferrite comes from the enhanced orbital magnetic moments along the out-of-plane [001] direction through in-plane charge distribution by tensile strain, which adds the material functionalities in spinel ferrite thin films from the viewpoint of strain and orbital magnetic moments.

DOI: [10.1103/PhysRevB.105.134416](https://doi.org/10.1103/PhysRevB.105.134416)

Perpendicular magnetic anisotropy (PMA) is one of the crucial issues in the spintronics research field from the viewpoints of thermal stability enhancement and high-density storage technology with low current magnetization switching. Tremendous efforts have been devoted to design materials with large PMA to add novel functionalities and external field control of magnetic properties [1–5]. Among these materials, the magnetic oxides possess a number of attractive advantages for use in spintronics devices because of their semiconducting or insulating behavior with high spin polarization. These magnetic oxides can be utilized for their spin-filtering effects, resulting in high tunnel magnetoresistance with multiferroic properties by controlling the tensile or compressive strains in the thin films [6–8].

The most famous spinel-type compounds for spintronics applications might be Co-ferrite ( $\text{CoFe}_2\text{O}_4$ ; CFO) epitaxial thin films because of their insulating advantages and spin filtering, high-frequency performance, and magnetostrictive properties [9–16]. Furthermore, the interfacial proximity effect, emerging on films with nonmagnetic heavy-metal elements which possess a large atomic spin-orbit interaction [17–19], also develops, as shown by spin-orbitronics research, through interfacial spin-orbit coupling. Recent development appends further functionality of large PMA in CFO on the order of  $10^6$  J/m<sup>3</sup> by tuning the Co compositions [20–23]. Since CFO exhibits a high magnetostriction coefficient ( $\lambda_{100} = -590 \times 10^{-6}$ ), the strain from the substrates propagates into the CFO layer, which brings the local distortion around the transition-metal (TM) cation sites. In fact, the lattice mismatch between MgO (4.21 Å) and CFO (8.38 Å) forming almost a double period brings the epitaxial crystalline growth with a few percentages of tensile strain

into the CFO thin layer. Depending on the Co compositions, the lattice constants of CFO can be tuned systematically. Structural and magnetic properties in the CFO thin films can be controlled by the cation vacancies and antiphase boundaries which are generated during the crystalline growth and suppress the saturation magnetization values through the antiparallel spin coupling [24–27]. Historically, magnetic anisotropy in bulk CFO has been understood as an effect whereby the average of  $\langle 111 \rangle$  easy-axis directions produces cubic anisotropy in  $\text{Co}^{2+}$  [28–30]. Recent theoretical and experimental investigations for CFO thin films suggest that the tensile strain into the CFO layer produces the PMA [31–38]. The squareness of out-of-plane hysteresis curves depends on the growth mode, such as molecular-beam epitaxy, pulsed-laser deposition (PLD), or sputter deposition. It is also reported that the PMA increases in off-stoichiometric CFO films with low Co compositions [22,23]. Although the PMA in CFO is strongly demanded for spinel-type oxide spintronics and spin-orbitronics by controlling the orbital states [39], the microscopic origin of the PMA appearing in the low Co compositions of CFO has not been clarified yet.

In order to understand the PMA in CFO, the element-specific orbital magnetic moments  $m_{\text{orb}}$  and their orbital anisotropy have to be examined explicitly. In particular,  $m_{\text{orb}}$  is expected to be sensitive to the strain and local symmetry from the ligand fields around the TM ions. X-ray magnetic circular and linear dichroisms (XMCD and XMLD) with their magneto-optical sum rules are powerful tools to detect the element-specific spin and orbital states in each site with the charge asphericity [40]. Especially, XMLD sum rules can probe the orbital anisotropy ( $Q = 3L_z^2 - L^2$ ) in the notation of orbital angular momentum  $L$  and electric quadrupoles  $Q$ .

Furthermore, since the Fe *L*-edge spectra consist of the signals of three kinds of Fe<sup>2+</sup> or Fe<sup>3+</sup> states with octahedral  $O_h$  and tetrahedral  $T_d$  symmetries, the XMCD and XMLD magneto-optical sum rules for the integrals of Fe *L*-edge spectra cannot be adopted without separating each contribution. Site- and state-resolved analyses take on a crucial role for understanding the origin of PMA. For the analysis of XMCD and XMLD spectra, ligand-field multiplet (LFM) cluster-model simulations including the configuration interaction (CI) approach are used to determine the site-specific electronic structure parameters accompanied by spin and orbital magnetic moments and their anisotropies [41]. XMCD and XMLD for CFO with in-plane anisotropy have been extensively studied with the angular dependence between the incident polarized beam, magnetic field, and sample surface normal [42–45]. However, x-ray magnetic spectroscopy investigations for PMA films with square magnetization–magnetic field (*M*-*H*) hysteresis shape in low Co compositions have not been pursued. We have performed XMLD measurements to probe the orbital anisotropy in several PMA systems by using remanent magnetization states in the polar Kerr geometry [46,47]. On the other hand, the recent operando-XMCD technique enables manipulation of out-of-plane and in-plane  $m_{\text{orb}}$  by controlling strain in the magnetic multilayers, which is a microscopic origin of magnetostriction; that leads to the observation of an effect proposed as the “orbital-striction effect” [48]. The PMA in strained CFO can be also categorized as a novel orbital-controlled material system by using the orbital degeneracy in the Co<sup>2+</sup>  $3d^7$  system in the  $O_h$  ligand field. Furthermore, extended x-ray absorption fine structure (EXAFS) analysis through the multiple-scattering process is also employed to determine the element-specific structural characterization. The precise determinations of spin and orbital states become a key solution to develop a strain-induced orbital physics and their applications using CFO.

In this paper, considering the above research motivations, we aim to investigate the origin of PMA in CFO from the viewpoint of element-specific spin and orbital magnetic moments and their anisotropy using XMCD and XMLD with LFM calculations and local structure detection by EXAFS analysis.

The Co<sub>*x*</sub>Fe<sub>3-*x*</sub>O<sub>4+ $\delta$</sub>  (001) samples ( $x = 0.2$  and  $0.6$ ) were prepared by PLD on MgO (001) substrates with a similar recipe to that used in Ref. [23]. The PLD was performed under the conditions of a substrate temperature of 300 °C, a background oxygen pressure of 6.0 Pa, and a deposition rate of 0.03 nm/s. A neodymium-doped yttrium-aluminum-garnet laser at double frequency (532 nm) with a pulse width of 6 ns and a repetition rate of 30 Hz was used. The energy density of the laser beam was controlled to 1 J/cm<sup>2</sup> by an optical lens. The 13-nm-thick CFO (001) layer with 1-nm-thick Cu capping layer was deposited for various Co compositions  $x$ . Excess oxygens accompanied by possible cation vacancies are described as  $\delta$ . The case of  $x = 0.2$  and  $0.6$  exhibits the PMA and in-plane anisotropy, respectively. The in-plane anisotropy in Co<sub>0.6</sub>Fe<sub>2.4</sub>O<sub>4+ $\delta$</sub>  is produced by the postannealing at 400 °C after the growth by releasing the strain. The results of sample characterization by x-ray diffraction (XRD) and magnetization measurements are shown in the Supplemental Material (Fig. S1) [49].

Measurements of XMCD and XMLD were performed at BL-7A and BL-16A in the Photon Factory at the High-Energy Accelerator Research Organization (KEK-PF). For the XMCD measurements, the photon helicity was fixed, and a magnetic field of  $\pm 1.2$  T was applied parallel to the incident polarized soft x-ray beam, to obtain signals defined as  $\mu+$  and  $\mu-$  spectra. The total electron yield mode was adopted, and all measurements were performed at room temperature. The x-ray absorption spectroscopy (XAS) and XMCD measurement geometries were set to normal incidence, so that the directions of the photon helicity axis and the magnetic field were parallel and normal to the surface, enabling measurement of the absorption processes involving the normal components of the spin and orbital magnetic moments. In the XMLD measurements, the remanent states magnetized out of plane were adopted. For grazing incident measurements in XMLD, the tilting angle between the incident beam and the sample surface normal was kept at 60°. The direction of the electric field **E** of the incident linearly polarized synchrotron beam was tuned horizontally and vertically by an undulator. We define the sign of XMLD by the subtraction of the (**M**||**E**) – (**M**⊥**E**) spectra with respect to the magnetization **M**. The EXAFS measurements at the Co *K* edge were performed at BL-12C at KEK-PF using the fluorescence yield mode with a 19-element solid-state detector at room temperature.

Figure 1 shows the XAS and XMCD of Co<sub>0.2</sub>Fe<sub>2.8</sub>O<sub>4+ $\delta$</sub>  for Fe and Co *L* edges with the normal incidence setup. Spectra are normalized at each absorption edge. Because of the composition ratio of Co : Fe = 1 : 14, the XAS intensities of Co are suppressed. The XMCD intensity ratio to XAS is estimated to be 5 and 47% for the Fe and Co *L*<sub>3</sub> edge, respectively. The raw data are displayed in the Supplemental Material (Fig. S2). XAS and XMCD line shapes for Fe *L* edges show distinctive features due to the three kinds of Fe states (Fe<sup>3+</sup> in  $O_h$ , Fe<sup>3+</sup> in  $T_d$ , and Fe<sup>2+</sup> in  $O_h$ ). For the Fe *L* edges, although the difference in XAS is small, clear differential XMCD line shapes are detected. The Fe<sup>3+</sup> state with  $T_d$  symmetry exhibits opposite sign, which is common for the spinel ferrite compounds. On the other hand, in the case of Fe<sub>3</sub>O<sub>4</sub>, the Fe<sup>2+</sup> component is more enhanced [50]. Large XMCD signals in the Co *L* edge correspond to the saturated magnetized states. Within the orbital sum rule, the large  $m_{\text{orb}}$  gives rise to the asymmetric XMCD line shapes. Since the Co site is almost identical to Co<sup>2+</sup> ( $O_h$ ) symmetry, the sum rules can be applicable for the Co XMCD spectra. The spin and orbital magnetic moments for Co<sup>2+</sup> sites are estimated as  $1.32 \pm 0.20$  and  $0.63 \pm 0.09 \mu_B$ , respectively, using an electron number of 7.1. The error bars mainly originate from the estimation of background in XAS which is used for the sum rule analysis. Large  $m_{\text{orb}}$  originates from the orbital degeneracy in the  $d^7$  electron system in the strained Co site. The multiplet structures are almost similar to the previous report by the LFM calculations along the easy-axis direction [44,45]. In order to confirm the PMA, the element-specific magnetic hysteresis curves are measured at each peak in the Fe and Co *L*<sub>3</sub> edge. As shown in Fig. 1(c), clear square shapes are detected at each of the photon energies due to the out-of-plane easy axis, which is almost consistent with the magnetization measurement shown in Fig. S1 [49]. The square *M*-*H* curves for all energies suggest the strong exchange coupling

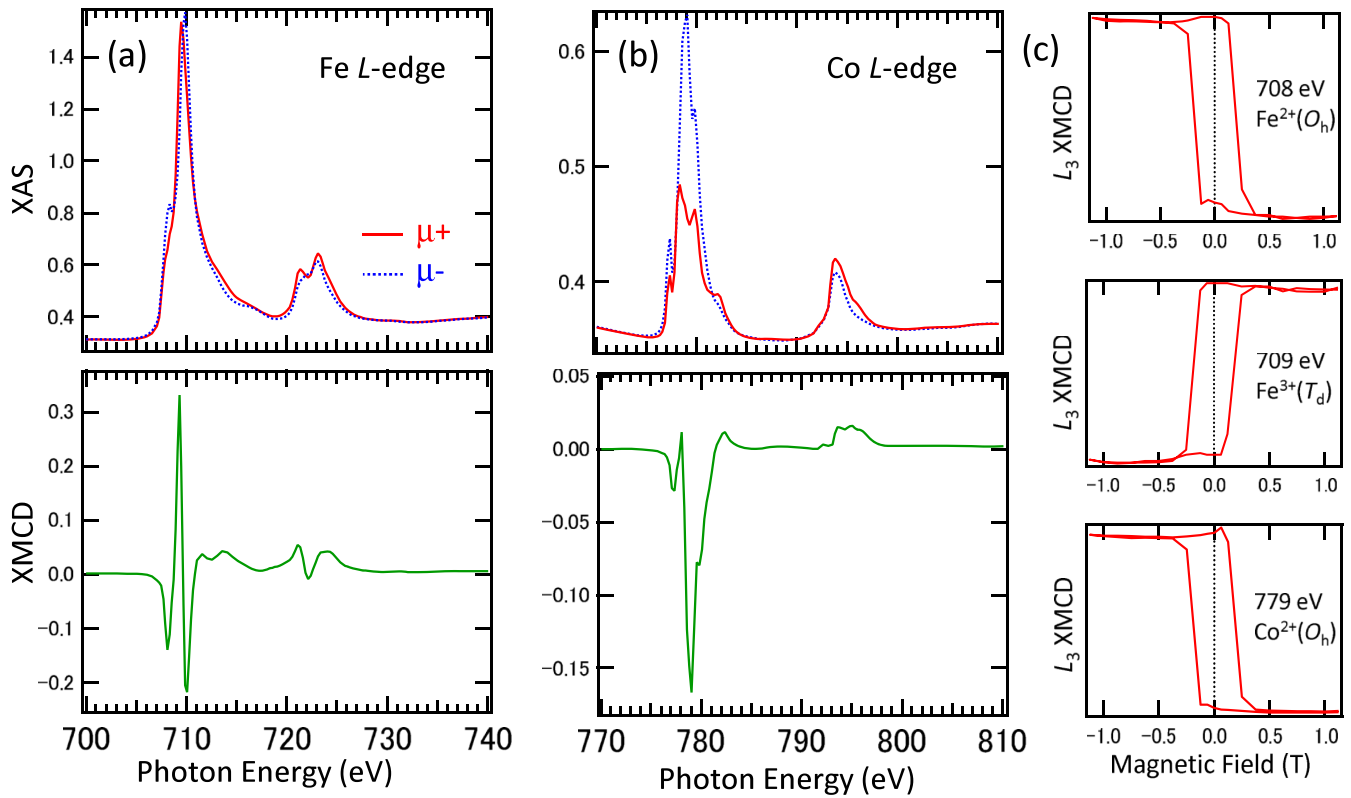


FIG. 1. XAS and XMCD of  $\text{Co}_{0.2}\text{Fe}_{2.8}\text{O}_{4+\delta}$  film.  $\mu^+$  and  $\mu^-$  in XAS denote the magnetic field direction along the incident photon beams at normal incident geometry. The difference  $\mu^+ - \mu^-$  is defined as XMCD spectra for the (a) Fe  $L$  edge and (b) Co  $L$  edge. Both XAS and XMCD intensities are normalized by the photon flux. (c) Magnetic field dependence at each fixed photon energy, 708, 709, and 779 eV, corresponding to  $\text{Fe}^{2+}$  ( $O_h$ ),  $\text{Fe}^{3+}$  ( $T_d$ ), and  $\text{Co}^{2+}$  ( $O_h$ ) peaks, respectively.

among each of the sites. The opposite sign in the  $M$ - $H$  curves at the  $\text{Fe}^{3+}$   $T_d$  site and the  $\text{Fe}^{2+}/\text{Co}^{2+}$   $O_h$  sites originates from the antiferromagnetic superexchange interaction among these sites. These findings suggest that the small amounts of anisotropic Co sites with large  $m_{\text{orb}}$  govern the easy-axis direction of Fe sites and stabilize the PMA.

Figure 2 shows the  $\mathbf{E}$  vector polarization dependent XAS, where the electric field  $\mathbf{E}$  is parallel and perpendicular to the out-of-plane magnetization direction. The differential line shapes were similar to those of previously reported spectra [44]. Because of the small difference in XAS by the horizontal (parallel) and vertical (perpendicular) beams as shown in the inset of Fig. 2(a), XMLD intensities are also suppressed and displayed in the different scales. For Fe  $L$ -edge XMLD, the overlapping of three kinds of components brings a complex differential line shape. We note that the integrals of the XMLD line shapes are proportional to the charge asphericity within the XMLD sum rule [51]. For Co  $L$ -edge XMLD of the  $\text{Co}^{2+}$   $O_h$  site, we confirmed that the integral of XMLD converges to a negative value, deducing that the sign of  $Q_{zz}$ , where  $Q_{zz}$  is the diagonal tensor component of the electric quadrupole moment describing the charge distribution asphericity as  $Q_{xx} + Q_{yy} + Q_{zz} = 0$ , is negative with an order of  $10^{-1}$ . The result means that the in-plane orbital states are strongly coupled with  $\mathbf{E}$ . This value can be also estimated from the XMCD spin sum rule considering the magnetic dipole  $m_T$  term. Since the measurement geometry of  $60^\circ$  tilted from the sample surface normal

cannot detect the precise orthogonal direction, the oblique angle suppresses the linear dichroism intensity to  $\sqrt{3}/2$ . The orbital polarization of Co  $3d$  states means that there is a pancake-type oblate charge distribution, which enhances the out-of-plane component of  $m_{\text{orb}}$ . Therefore, with both XMCD and XMLD combined, it can be concluded that the in-plane tensile strain triggers the changes in charge distribution along the in-plane direction, resulting in the large out-of-plane  $m_{\text{orb}}$  and the PMA.

For the analysis of XMCD and XMLD spectra, we employed cluster-model calculations including the CI for  $\text{Co}^{2+}$  and Fe sites in  $\text{Co}_{0.2}\text{Fe}_{2.8}\text{O}_{4+\delta}$  as tetrahedral ( $T_d$ )  $\text{TMO}_4$  and octahedral ( $O_h$ )  $\text{TMO}_6$  clusters, modeled as a fragment of the spinel-type structures. The Hamiltonian included the electronic structure parameters of full on-site TM  $3d$ - $3d$  (valence-valence) and  $2p$ - $3d$  (core-valence) Coulomb interactions  $U$  and the  $T_d$  or  $O_h$  crystal fields ( $10Dq$ ) in the TMs, along with the hybridization between the TM  $3d$  and O  $2p$  wave functions. The charge-transfer energy was defined as  $\Delta = E(3d^{n+1}\underline{L}) - E(3d^n)$ , where  $\underline{L}$  denotes a hole in a ligand  $p$  orbital. The hybridization between the TM  $3d$  and O  $2p$  states was also parametrized in terms of the Slater-Koster parameters ( $pd\sigma$ ) and ( $pd\pi$ ), where the relation ( $pd\sigma$ ) =  $-1/2(pd\pi)$  was used [52]. The parameters ( $pp\sigma$ ) and ( $pp\pi$ ) were always set to zero. In all cases, a Gaussian broadening was used to simulate spectral broadening.

As shown in Fig. 3, spectral line shapes of XMCD and XMLD can be reproduced by the LFM calculations

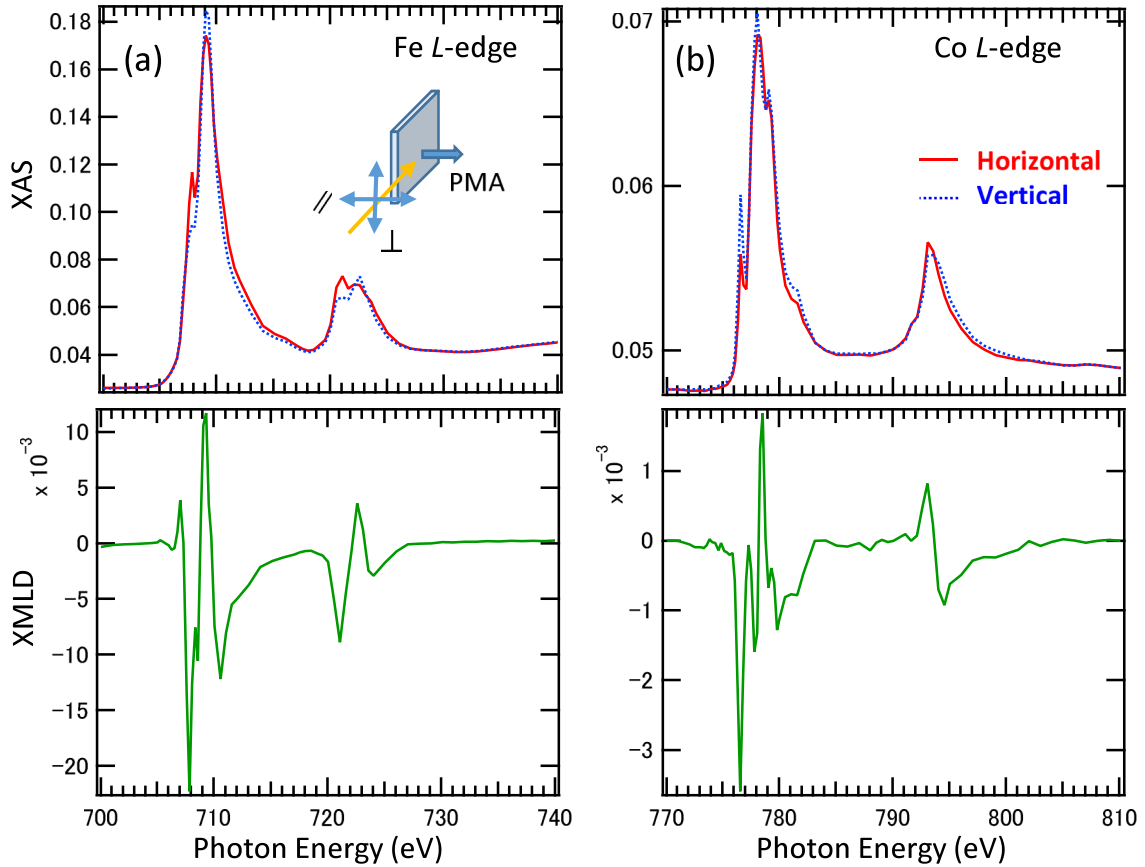


FIG. 2. XAS and XMLD of  $\text{Co}_{0.2}\text{Fe}_{2.8}\text{O}_{4+\delta}$  film of (a) Fe and (b) Co  $L$  edges. Spectra were taken at the grazing incident setup, where  $\mathbf{E}$  of the incident beam and direction of magnetization  $\mathbf{M}$  were parallel (horizontal) and perpendicular (vertical), respectively. The inset in (a) displays an illustration of the XMLD measurement geometry.

qualitatively, at least the peak positions, with three Fe states and a uniform Co state. The fitting parameters are listed in Table I. We emphasize that the same adjusted parameters of  $\Delta$ ,  $U$ , and  $pd\sigma$  and intensity ratios of each component for XMCD and XMLD are applicable for the fitting. In comparison with the previous first-principles calculations of CFO, the values of  $U = 5$  eV are also plausible from the viewpoint of LFM calculations [53–56]. The multiplet parameter values are almost similar to the previous report [57]. For the  $\text{Co}^{2+} 3d^7$  case, the  $t_{2g}$  states are split into two levels by the tetragonal distortion, and the lowest  $xy$  states are occupied by one of the down-spin electrons. The other electron occupies the degenerated  $yz$  or  $zx$  states [35]. We determined the tetragonal distortion for the Co  $3d$  states ( $D_{\text{tet}}$ ) to be 0.02 eV in order to reproduce the XMCD and XMLD spectral line shapes qualitatively. However, the best-fit parameter sets shown in Table I are not sensitive to the

TABLE I. The electronic structure parameters used in the LFM cluster calculation. Values are given in eV.

	$\Delta$	$U$	$(pd\sigma)$	$10Dq$
$\text{Fe}^{2+} (O_h)$	6.5	6.0	1.2	0.9
$\text{Fe}^{3+} (O_h)$	0.5	6.0	1.2	0.9
$\text{Fe}^{3+} (T_d)$	4.5	6.0	2.0	-0.5
$\text{Co}^{2+} (O_h)$	6.5	6.0	1.3	0.5

parameters caused by the strain. The intensity ratio of  $\text{Fe}^{3+} T_d$ ,  $\text{Fe}^{3+} O_h$ , and  $\text{Fe}^{2+} O_h$  is deconvoluted to be 1 : 1.3 : 0.25 in the fitting of Fe  $L_{3-}$  edge XMCD and XMLD affecting the decrease of  $\text{Fe}^{2+}$  states in the inverse spinel structure. The Co  $L$ -edge line shapes are reproduced with only a single  $\text{Co}^{2+}$  site, except the peak at 779.5 eV in XMLD.

In order to confirm the local environment around the Co atoms, XAFS measurements with EXAFS analysis in the Co  $K$  edge were performed to deduce the nearest-neighbor distance through the Fourier transform. As shown in Fig. 4, the Co  $K$ -edge absorption spectra with EXAFS oscillatory behaviors are observed for  $x = 0.2$  (PMA) and  $x = 0.6$  (in-plane anisotropy). We note that the Fe  $K$ -edge XAFS cannot be separated in the Fourier transform without some assumption because of the contributions of three kinds of states. Clear XAFS oscillation is detected and plotted in the wave number  $k$  in the inset of Fig. 4(a). The XAFS oscillation function  $k^3\chi(k)$  can be fitted by the FEFF8 program [58], and the Fourier transformed EXAFS profile is also displayed in Fig. 4(b) considering the information up to the second-nearest neighbor from the Co site. By using the fitting procedure, the nearest Co-O bond length in the Co sites is 2.09 and 2.08 Å for the PMA and in-plane cases, respectively, which is almost identical to the previous study [59]. The expansion of the nearest neighbor in the PMA film is qualitatively consistent with the XRD shown in Fig. S1 [49]. Because of the effect of phase

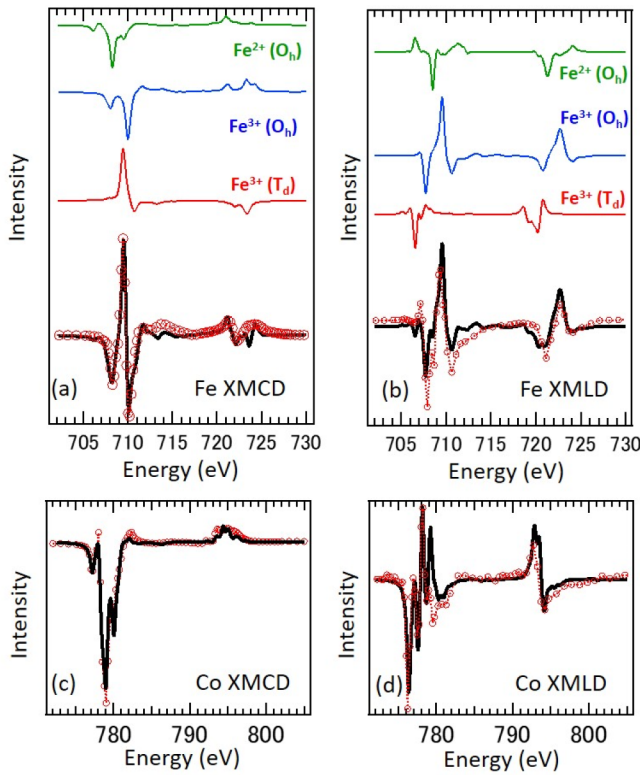


FIG. 3. Calculated XMCD and XMLD spectra for (a) and (b) Fe and (c) and (d) Co  $L$  edges. For the Fe  $L$  edge, three components, the  $\text{Fe}^{2+}(\text{O}_h)$ ,  $\text{Fe}^{3+}(\text{O}_h)$ , and  $\text{Fe}^{3+}(\text{T}_d)$  sites, are also shown. Total spectra are shown as black solid curves. Curves with open circles are the experimental XMCD and XMLD shown in Figs. 1 and 2.

shift, the peak position in EXAFS is not related to the bond length directly. The coordination number also becomes large in the case of PMA because of the distorted local environment around the Co site, which corresponds to the intensity of the EXAFS profile in Fig. 4(b). These findings suggest that the tensile local distortion triggers the PMA in the Co site of strained CFO.

Considering the above results, we discuss the electronic structures of CFO. First, we discuss the suppression of  $\text{Fe}^{2+}$  with increasing Co composition. A previous report of Mössbauer spectra for a related CFO with PMA suggests the suppression of  $\text{Fe}^{2+}$  [23]; in that study,  $\sim 100$  nm from the interface were probed using incident  $\gamma$  rays and emitted conversion electrons. Since the probing depth region of XMCD is 3 nm beneath the surface, finite  $\text{Fe}^{2+}$  states in XMCD are located in the surface region. A previous report suggests that the  $\text{Fe}^{2+}$  state is located in the surface region with inevitable lateral inhomogeneity [60].

Second, we discuss the occupation of cation sites by the charge neutrality and the number of cation elements. Using the Co concentration and charge neutrality in the inverse spinel structure of the formation of a spinel structure of  $\text{AB}_2\text{O}_4$  formula units,  $\text{Fe}^{3+}(\text{T}_d)(\text{Co}^{2+}(\text{O}_h)\text{Fe}^{2+}(\text{O}_h)\text{Fe}^{3+}(\text{O}_h))\text{O}_4$ , the following two equations are deduced for  $\text{Co}_{0.2}\text{Fe}_{2.8}\text{O}_{4+\delta}$ :  $14n_{\text{Co}^{2+}} = n_{\text{Fe}^{2+}} + n_{\text{Fe}^{3+}}$  and  $2n_{\text{Co}^{2+}} + 2n_{\text{Fe}^{2+}} + 3n_{\text{Fe}^{3+}} = 8$ , where  $n$  is the number of each element and the cation vacancy is implicitly incorporated as  $\delta$ . Since the ratio of

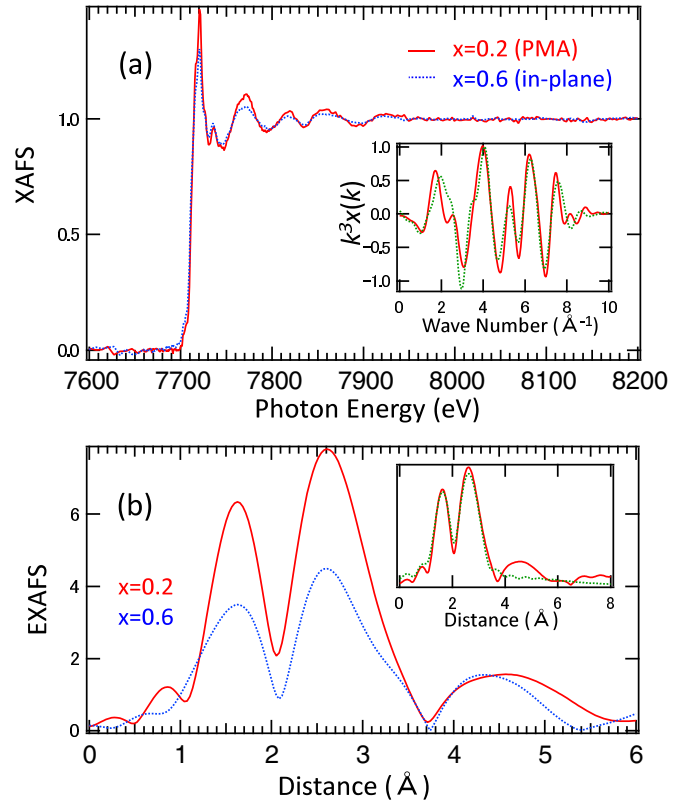


FIG. 4. XAFS and EXAFS of  $\text{Co}_{0.2}\text{Fe}_{2.8}\text{O}_{4+\delta}$  (PMA) and  $\text{Co}_{0.6}\text{Fe}_{2.4}\text{O}_{4+\delta}$  (in-plane anisotropy). (a) Co  $K$ -edge XAFS. The inset shows the corresponding  $k$  oscillation in  $k^3\chi(k)$  for  $x = 0.2$ . The dotted curve shows the fitting result. (b) EXAFS profile after the Fourier transform. The inset shows the fitting result for  $x = 0.2$ .

$n_{\text{Fe}^{3+}(\text{T}_d)}$ ,  $n_{\text{Fe}^{2+}(\text{O}_h)}$ , and  $n_{\text{Fe}^{3+}(\text{O}_h)}$  is estimated from the XMCD and XMLD analyses, these four parameters are calculated to be  $n_{\text{Fe}^{3+}(\text{O}_h)} = 1.34$ ,  $n_{\text{Fe}^{3+}(\text{T}_d)} = 1.03$ ,  $n_{\text{Fe}^{2+}(\text{O}_h)} = 0.26$ , and  $n_{\text{Co}^{2+}(\text{O}_h)} = 0.19$ . These findings suggest that the existence of excess cation vacancies  $n_v$  can be estimated to be 0.185 from the equation for the cation site,  $n_v = 3 - n_{\text{Fe}^{3+}(\text{O}_h)} - n_{\text{Fe}^{3+}(\text{T}_d)} - n_{\text{Fe}^{2+}(\text{O}_h)} - n_{\text{Co}^{2+}(\text{O}_h)}$ . We emphasize that the cation vacancy can be estimated quantitatively from the analysis of XMCD.

Third, we discuss the relationship between strain and orbital magnetic moments. For the  $\text{Co}^{2+} 3d^7$  system, the ground-state  $^4F$  multiplet energy split by the cubic crystal field to the  $\Gamma_4$  state, and further effects by the trigonal or tetragonal field and exchange coupling stabilize the lowest  $3d^7$  states. The splitting of the  $t_{2g}$  state promotes the degeneracy for spins as analogous to the  $3d^2$  system of spinel-type  $\text{V}^{3+}$  compounds [61,62]. Large  $m_{\text{orb}}$  is recovered by the spin-orbit coupling  $\xi_{\text{Co}}$  of 70 meV. Since the uniaxial anisotropy in spinel-type Co ferrite is inevitably formed from the structural and electronic configuration, the out-of-plane easy axis can originate from the tensile strain effect. In the theoretical model calculation, the PMA energy  $K$  deduced from the energy difference along the axis direction can be expressed as  $K = E(100) - E(001) = -B_1\chi$ , where  $B_1$  and  $\chi$  are the magnetoelastic coefficient and strain, respectively [34]. A phenomenological  $B_1$  of  $1.4 \times 10^8 \text{ J/m}^3$  consists of the elastic constant and magnetostriction coefficient at room

temperature for  $\text{CoFe}_2\text{O}_4$ . In the case of  $x = 0.2$ ,  $B_1x$  is applied to estimate  $K$ . Considering the lattice constants of  $a_{\parallel} = 8.42 \text{ \AA}$  and  $a_{\perp} = 8.29 \text{ \AA}$  estimated from the XRD, a strain of  $(a_{\parallel} - a_{\perp})/a_0 \sim 1.5\%$  was deduced using the bulk CFO value  $a_0 = 8.38 \text{ \AA}$  [32]. Therefore the PMA energy is roughly estimated to be  $0.51 \times 10^6 \text{ J/m}^3$ . On the other hand, microscopic estimation of the PMA energy can be performed using anisotropic  $m_{\text{orb}}$  as  $K = 1/4\xi\Delta m_{\text{orb}}$ , where the spin-orbit coupling constant is  $\xi$  and  $\Delta m_{\text{orb}}$  is the difference between out-of-plane and in-plane  $m_{\text{orb}}$ . Although the in-plane  $m_{\text{orb}}$  cannot be detected unless applying high magnetic field to saturate the magnetization along the hard axis, we used the value in Ref. [44] with extrapolation to the case of low Co concentration. Assuming the value of  $\Delta m_{\text{orb}}$  to be  $0.2 \mu_B$ , the PMA energy of Co can be estimated to be  $1.6 \times 10^6 \text{ J/m}^3$  with the assumption of the Co composition  $x = 0.2$  and strained CFO volume. The value of  $K$  from XMCD is overestimated compared with that from magnetization measurements, in general, by a prefactor of 0.1 [63]. These estimations suggest that the PMA energy can be explained mainly by the contribution of a small amount of anisotropic Co sites. Furthermore, the macroscopic magnetostriction effect, which is the relation between strain and  $K$ , can be recognized including the  $m_{\text{orb}}$  from the viewpoint of electron theory as the orbital-elastic effect. The contributions from the  $\text{Fe}^{3+} (3d^5)$  sites are negligible because of half-filled quenched orbital magnetic moments. The contribution from the  $\text{Fe}^{2+} (3d^6)$  sites is also quenched since the strained undegenerated level is occupied. Therefore the origin of PMA in  $\text{Co}_{0.2}\text{Fe}_{2.8}\text{O}_{4+\delta}$  can be predominantly explained by the enhanced  $m_{\text{orb}}$  of 1/14 Co compositions through the strained charge distributions, which can be recognized as diluted doped magnetic oxide systems.

Finally, we discuss the origin of PMA in the spinel-type oxides from the viewpoint of tensile or compressive strain and  $m_{\text{orb}}$ . The strain in CFO is derived from the tensile strain in the film, which is detected by the EXAFS analysis and confirmed

by the sign of XMLD. Recent reports show that the PMA in spinel-type  $\text{NiCo}_2\text{O}_4$  originates from the compressive strain in the film [64,65] and that the enhancement of  $m_{\text{orb}}$  in XMCD measurements is not distinctive with the 2+ and 3+ mixed valence states of both Co and Ni sites [66]. Therefore the PMA in spinel-type oxides can be categorized by the tensile or compressive strain. Because of tensile strain, oblate-type charge distribution induces  $m_{\text{orb}}$  along the out-of-plane direction, which is similar to the case of enhanced  $m_{\text{orb}}$  in the Co/Pd multilayer [67]. On the other hand, in-plane compression or out-of-plane elongation modulates the prorate-type charge distributions, which induces the quadrupole moments without enhancing  $m_{\text{orb}}$  as discussed in a strained  $\text{Mn}_{3-x}\text{Ga}$  system [47].

In summary, using XMCD and XMLD, we investigated the element-specific orbital magnetic moments and their anisotropy in Co-ferrite thin films with low Co concentration which exhibit PMA. The origin of PMA in CFO is explained by the large  $m_{\text{orb}}$  in the  $\text{Co}^{2+} (3d^7)$  states. The tensile lattice strain, which is deduced from EXAFS, induces the out-of-plane  $m_{\text{orb}}$  through the anisotropic in-plane charge distribution. Furthermore, a method to estimate the number of cation vacancies from XMCD line shapes was also proposed. Our finding clearly reveals that the controlling strain modulates  $m_{\text{orb}}$ , which opens up the material functionalities in the oxide spin-orbitronics by strain engineering, especially in TM  $d^7$  systems.

This work was partially supported by JSPS KAKENHI (Grant No. 16H06332), the Kato Science and Technology Foundation, the Izumi Science and Technology Foundation, and the Telecommunications Advancement Foundation. Parts of the synchrotron radiation experiments were performed under the approval of the Photon Factory Program Advisory Committee, KEK (No. 2019G028 and No. 2021G069).

- 
- [1] S. Mangin, D. Ravelosona, J. A. Katine, M. J. Carey, B. D. Terris, and E. E. Fullerton, Current-induced magnetization reversal in nanopillars with perpendicular anisotropy, *Nat. Mater.* **5**, 210 (2006).
  - [2] S. Ikeda, K. Miura, H. Yamamoto, K. Mizunuma, H. D. Gan, M. Endo, S. Kanai, J. Hayakawa, F. Matsukura, and H. Ohno, A perpendicular anisotropy  $\text{CoFeB/MgO}$  magnetic tunnel junction, *Nat. Mater.* **9**, 721 (2010).
  - [3] W.-G. Wang, M. Li, S. Hageman, and C. L. Chien, Electric-field-assisted switching in magnetic tunnel junctions, *Nat. Mater.* **11**, 64 (2012).
  - [4] T. Nozaki, A. Koziol-Rachwal, M. Tsujikawa, Y. Shiota, X. Xu, T. Ohkubo, T. Tsukahara, S. Miwa, M. Suzuki, S. Tamaru, H. Kubota, A. Fukushima, K. Hono, M. Shirai, Y. Suzuki, and S. Yuasa, Highly efficient voltage control of spin and enhanced interfacial perpendicular magnetic anisotropy in iridium-doped  $\text{Fe/MgO}$  magnetic tunnel junctions, *NPG Asia Mater.* **9**, e451 (2017).
  - [5] B. Dieny and M. Chshiev, Perpendicular magnetic anisotropy at transition metal/oxide interfaces and applications, *Rev. Mod. Phys.* **89**, 025008 (2017).
  - [6] C. A. F. Vaz, Electric field control of magnetism in multiferroic heterostructures, *J. Phys.: Condens. Matter* **24**, 333201 (2012).
  - [7] T. Taniyama, Electric-field control of magnetism via strain transfer across ferromagnetic/ferroelectric interfaces, *J. Phys.: Condens. Matter* **27**, 504001 (2015).
  - [8] D. C. Vaz, A. Barthelemy, and M. Bibes, Oxide spin-orbitronics: New routes towards low-power electrical control of magnetization in oxide heterostructures, *Jpn. J. Appl. Phys.* **57**, 0902A4 (2018).
  - [9] A. V. Ramos, M.-J. Guittet, and J.-B. Moussy, R. Mattana, C. Deranlot, and F. Petroff, and C. Gatel, Room temperature spin filtering in epitaxial cobalt-ferrite tunnel barriers, *Appl. Phys. Lett.* **91**, 122107 (2007).
  - [10] Y. K. Takahashi, S. Kasai, T. Furubayashi, S. Mitani, K. Inomata, and K. Hono, High spin-filter efficiency in a Co ferrite fabricated by a thermal oxidation, *Appl. Phys. Lett.* **96**, 072512 (2010).
  - [11] N. M. Caffrey, D. Fritsch, T. Archer, S. Sanvito, and C. Ederer, Spin-filtering efficiency of ferrimagnetic spinels  $\text{CoFe}_2\text{O}_4$  and  $\text{NiFe}_2\text{O}_4$ , *Phys. Rev. B* **87**, 024419 (2013).

- [12] M. Foerster, M. Iliev, N. Dix, X. Marti, M. Barchuk, F. Sanchez, and J. Fontcuberta, The poisson ratio in  $\text{CoFe}_2\text{O}_4$  spinel thin films, *Adv. Funct. Mater.* **22**, 4344 (2012).
- [13] M. Scigaj, N. Dix, J. Gazquez, M. Varela, I. Fina, N. Domingo, G. Herranz, V. Skumryev, J. Fontcuberta, and F. Sanchez, Monolithic integration of room temperature multifunctional  $\text{BaTiO}_3$ - $\text{CoFe}_2\text{O}_4$  epitaxial heterostructures on  $\text{Si}(001)$ , *Sci. Rep.* **6**, 31870 (2016).
- [14] Y. Zhang, L. Shen, M. Liu, X. Li, X. Lu, L. Lu, C. Ma, C. You, A. Chen, C. Huang, L. Chen, M. Alexe, and C.-L. Jia, Flexible quasi-two-dimensional  $\text{CoFe}_2\text{O}_4$  epitaxial thin films for continuous strain tuning of magnetic properties, *ACS Nano* **11**, 8002 (2017).
- [15] K. Prabakar, R. Ranjith, P. Saravanana, and A. Srinivasa, Effect of magnetic field annealing on the magnetostriction and deflection properties of  $\text{CoFe}_2\text{O}_4$  thin films grown by PLD, *J. Magn. Magn. Mater.* **475**, 276 (2019).
- [16] H. Onoda, H. Sukegawa, J.-I. Inoue, and H. Yanagihara, Strain engineering of magnetic anisotropy in epitaxial films of cobalt ferrite, *Adv. Mater. Interfaces* **8**, 2101034 (2021).
- [17] Y. Hui, W. Cheng, Z. Zhang, H. Wang, C. Xie, and X. Miao, Transport mechanism of the magnetoresistance effects in  $\text{Ta}/\text{CoFe}_2\text{O}_4$  nanostructures, *Appl. Phys. Lett.* **110**, 192404 (2017).
- [18] H. B. Vasili, M. Gamino, J. Gazquez, F. Sanchez, M. Valvidares, P. Gargiani, E. Pellegrin, and J. Fontcuberta, Magnetoresistance in hybrid  $\text{Pt}/\text{CoFe}_2\text{O}_4$  bilayers controlled by competing spin accumulation and interfacial chemical reconstruction, *ACS Appl. Mater. Interfaces* **10**, 12031 (2018).
- [19] W. Amamou, I. V. Pinchuk, A. H. Trout, R. E. A. Williams, N. Antolin, A. Goad, D. J. O'Hara, A. S. Ahmed, W. Windl, D. W. McComb, and R. K. Kawakami, Magnetic proximity effect in  $\text{Pt}/\text{CoFe}_2\text{O}_4$  bilayers, *Phys. Rev. Materials* **2**, 011401(R) (2018).
- [20] H. Yanagihara, K. Uwabo, M. Minagawa, E. Kita, and N. Hirota, Perpendicular magnetic anisotropy in  $\text{CoFe}_2\text{O}_4$  (001) films epitaxially grown on  $\text{MgO}(001)$ , *J. Appl. Phys. (Melville, NY)* **109**, 07C122 (2011).
- [21] R. Comes, M. Gu, M. Khokhlov, J. Lu, and S. A. Wolf, Microstructural and domain effects in epitaxial  $\text{CoFe}_2\text{O}_4$  films on  $\text{MgO}$  with perpendicular magnetic anisotropy, *J. Magn. Magn. Mater.* **324**, 524 (2012).
- [22] T. Niizeki, Y. Utsumi, R. Aoyama, H. Yanagihara, J.-I. Inoue, Y. Yamasaki, H. Nakao, K. Koike, and E. Kita, Extraordinarily large perpendicular magnetic anisotropy in epitaxially strained cobalt-ferrite  $\text{Co}_x\text{Fe}_{3-2x}\text{O}_4$  (001) ( $x = 0.75, 1.0$ ) thin films, *Appl. Phys. Lett.* **103**, 162407 (2013).
- [23] K. Naruse, M. Tanaka, K. Nomura, T. Taniguchi, S. Honda, T. Ono, and K. Mibu, Perpendicular magnetic anisotropy and tunneling conductivity of epitaxial cobalt-ferrite (001) films grown on nonmagnetic metal films, *J. Magn. Magn. Mater.* **475**, 721 (2019).
- [24] S. Celotto, W. Eerenstein, and T. Hibma, Characterization of anti-phase boundaries in epitaxial magnetite films, *Eur. Phys. J. B* **36**, 271 (2003).
- [25] A. V. Singh, B. Khodadadi, J. B. Mohammadi, S. Keshavarz, T. Mewes, D. S. Negi, R. Datta, Z. Galazka, R. Uecker, and A. Gupta, Bulk single crystal-like structural and magnetic characteristics of epitaxial spinel ferrite thin films with elimination of antiphase boundaries, *Adv. Mater. (Weinheim)* **29**, 1701222 (2017).
- [26] X. Wang, Z. Hu, S. Agrestini, J. Herrero-Martín, M. Valvidares, R. Sankar, F.-C. Chou, Y.-H. Chu, A. Tanaka, L. H. Tjeng, and E. Pellegrin, Evidence for largest room temperature magnetic signal from  $\text{Co}^{2+}$  in antiphase-free and fully inverted  $\text{CoFe}_2\text{O}_4$  in multiferroic-ferrimagnetic  $\text{BiFeO}_3$ - $\text{CoFe}_2\text{O}_4$  nanopillar thin films, *J. Magn. Magn. Mater.* **530**, 167940 (2021).
- [27] Z. Li, J. Lu, L. Jin, J. Rusz, V. Kocevski, H. Yanagihara, E. Kita, J. Mayer, R. E. Dunin-Borkowski, H. Xiang, and X. Zhong, Atomic structure and electron magnetic circular dichroism of individual rock salt structure antiphase boundaries in spinel ferrites, *Adv. Funct. Mater.* **31**, 2008306 (2021).
- [28] J. Slonczewski, Origin of magnetic anisotropy in cobalt-substituted magnetite, *Phys. Rev.* **110**, 1341 (1958).
- [29] M. Tachiki, Origin of the magnetic anisotropy energy of cobalt ferrite, *Prog. Theor. Phys.* **23**, 1055 (1960).
- [30] J. B. Goodenough, *Magnetism and the Chemical Bond* (Wiley, New York, 1963).
- [31] Y. Suzuki, G. Hu, R. B. van Dover, and R. J. Cava, Magnetic anisotropy of epitaxial cobalt ferrite thin films, *J. Magn. Magn. Mater.* **191**, 1 (1999).
- [32] A. Lisfi, C. M. Williams, L. T. Nguyen, J. C. Lodder, A. Coleman, H. Corcoran, A. Johnson, P. Chang, A. Kumar, and W. Morgan, Reorientation of magnetic anisotropy in epitaxial cobalt ferrite thin films, *Phys. Rev. B* **76**, 054405 (2007).
- [33] J. Inoue, H. Itoh, M. A. Tanaka, K. Mibu, T. Niizeki, H. Yanagihara, and E. Kita, Study of perpendicular magnetic anisotropy and magneto-elastic coupling in the first principles and phenomenology, *IEEE Trans. Magn.* **49**, 3269 (2013).
- [34] J.-I. Inoue, H. Yanagihara, and E. Kita, Magnetic anisotropy and magnetostriction in cobalt ferrite with lattice deformation, *Mater. Res. Express* **1**, 046106 (2014).
- [35] J.-I. Inoue, T. Niizeki, H. Yanagihara, H. Itoh, and E. Kita, Electron theory of perpendicular magnetic anisotropy of Co-ferrite thin films, *AIP Adv.* **4**, 027111 (2014).
- [36] M. A. Tanaka, K. Harada, M. Takemura, K. Mibu, and J. Inoue, Nonlinear strain dependence of magnetic anisotropy in  $\text{CoFe}_2\text{O}_4$  films on  $\text{MgO}(001)$  substrates, *J. Appl. Phys. (Melville, NY)* **115**, 17C101 (2014).
- [37] T. Tainosho, J.-I. Inoue, S. Sharmin, M. Takeguchi, E. Kita, and H. Yanagihara, Large negative uniaxial magnetic anisotropy in highly distorted Co-ferrite thin films, *Appl. Phys. Lett.* **114**, 092408 (2019).
- [38] J. Inoue, H. Onoda, and H. Yanagihara, Uniaxial magnetic anisotropy of transition metal oxides: role of local lattice deformation, *J. Phys. D: Appl. Phys.* **53**, 195003 (2020).
- [39] A. Manchon and A. Belabbes, Chapter One - Spin-orbitronics at transition metal interfaces, *Solid State Phys.* **68**, 1 (2018).
- [40] J. Stöhr, Exploring the microscopic origin of magnetic anisotropies with X-ray magnetic circular dichroism (XMCD) spectroscopy, *J. Magn. Magn. Mater.* **200**, 470 (1999).
- [41] F. de Groot and A. Kotani, *Core Level Spectroscopy of Solids* (CRC, Boca Raton, FL, 2008).
- [42] G. van der Laan, E. Arenholz, R. V. Chopdekar, and Y. Suzuki, Influence of crystal field on anisotropic x-ray magnetic linear dichroism at the  $\text{Co}^{2+}L_{2,3}$  edges, *Phys. Rev. B* **77**, 064407 (2008).
- [43] J. A. Moyer, C. A. F. Vaz, E. Negusse, D. A. Arena, and V. E. Henrich, Controlling the electronic structure of  $\text{Co}_{1-x}\text{Fe}_{2+x}\text{O}_4$  thin films through iron doping, *Phys. Rev. B* **83**, 035121 (2011).

- [44] J. A. Moyer, C. A. F. Vaz, D. A. Arena, D. Kumah, E. Negusse, and V. E. Henrich, Magnetic structure of Fe-doped  $\text{CoFe}_2\text{O}_4$  probed by x-ray magnetic spectroscopies, *Phys. Rev. B* **84**, 054447 (2011).
- [45] Y. K. Wakabayashi, Y. Nonaka, Y. Takeda, S. Sakamoto, K. Ikeda, Z. Chi, G. Shibata, A. Tanaka, Y. Saitoh, H. Yamagami, M. Tanaka, A. Fujimori, and R. Nakane, Electronic structure and magnetic properties of magnetically dead layers in epitaxial  $\text{CoFe}_2\text{O}_4/\text{Al}_2\text{O}_3/\text{Si}(111)$  films studied by x-ray magnetic circular dichroism, *Phys. Rev. B* **96**, 104410 (2017).
- [46] J. Okabayashi, Y. Iida, Q. Xiang, H. Sukegawa, and S. Mitani, Perpendicular orbital and quadrupole anisotropies at Fe/MgO interfaces detected by x-ray magnetic circular and linear dichroisms, *Appl. Phys. Lett.* **115**, 252402 (2019).
- [47] J. Okabayashi, Y. Miura, Y. Kota, Kazuya Z. Suzuki, A. Sakuma, and S. Mizukami, Detecting quadrupole: a hidden source of magnetic anisotropy for Manganese alloys, *Sci. Rep.* **10**, 9744 (2020).
- [48] J. Okabayashi, Y. Miura, and T. Taniyama, Strain-induced reversible manipulation of orbital magnetic moments in Ni/Cu multilayers on ferroelectric  $\text{BaTiO}_3$ , *npj Quantum Mater.* **4**, 21 (2019).
- [49] See Supplemental Material at <http://link.aps.org/supplemental/10.1103/PhysRevB.105.134416> for XRD, magnetization measurements, and wide-range XAS and XMCD spectra of  $\text{Co}_x\text{Fe}_{3-x}\text{O}_{4+\delta}$  ( $x = 0.2$  and  $0.6$ ).
- [50] S. Yasui, S. Honda, J. Okabayashi, T. Yanase, T. Shimada, and T. Nagahama, Large Inverse Tunnel Magnetoresistance in Magnetic Tunnel Junctions with an  $\text{Fe}_3\text{O}_4$  Electrode, *Phys. Rev. Appl.* **15**, 034042 (2021).
- [51] S. S. Dhesi, G. van der Laan, and E. Dudzik, Determining element-specific magnetocrystalline anisotropies using x-ray magnetic linear dichroism, *Appl. Phys. Lett.* **80**, 1613 (2002).
- [52] W. A. Harrison, *Electronic Structure and the Properties of Solids* (Dover, New York, 1989).
- [53] Z. Szotek, W. M. Temmerman, D. Kodderitzsch, A. Svane, L. Petit, and H. Winter, Electronic structures of normal and inverse spinel ferrites from first principles, *Phys. Rev. B* **74**, 174431 (2006).
- [54] Y. H. Hou, Y. J. Zhao, Z. W. Liu, H. Y. Yu, X. C. Zhong, W. Q. Qiu, D. C. Zeng, and L. S. Wen, Structural, electronic and magnetic properties of partially inverse spinel  $\text{CoFe}_2\text{O}_4$ : A first-principles study, *J. Phys. D: Appl. Phys.* **43**, 445003 (2010).
- [55] D. Das, R. Biswas, and S. Ghosh, Systematic analysis of structural and magnetic properties of spinel  $\text{CoFe}_2\text{O}_4$  ( $B = \text{Cr, Mn}$  and  $\text{Fe}$ ) compounds from their electronic structures, *J. Phys.: Condens. Matter* **28**, 446001 (2016).
- [56] S. M. Ansari, V. Kashid, H. Salunke, D. Sen, Y. D. Kolekar, and C. V. Ramana, First-principles calculations of the electronic structure and magnetism of nanostructured  $\text{CoFe}_2\text{O}_4$  microgranules and nanoparticles, *Phys. Rev. B* **102**, 035446 (2020).
- [57] H. Elnaggar, M. W. Haverkort, M. H. Hamed, S. S. Dhesi, and F. M. F. de Groot, Tensor description of X-ray magnetic dichroism at the Fe  $L_{2,3}$ -edges of  $\text{Fe}_3\text{O}_4$ , *J. Synchrotron Radiat.* **28**, 247 (2021).
- [58] A. L. Ankudinov, B. Ravel, J. J. Rehr, and S. D. Conradson, Real space multiple scattering calculation of XANES, *Phys. Rev. B* **58**, 7565 (1998).
- [59] S. A. Chambers Jr., R. F. C. Farrow, S. Maat, M. F. Toney, L. Folks, J. G. Catalanoc, T. P. Trainor, and G. E. Brown, Jr., Molecular beam epitaxial growth and properties of  $\text{CoFe}_2\text{O}_4$  on  $\text{MgO}(001)$ , *J. Magn. Magn. Mater.* **246**, 124 (2002).
- [60] M. Minagawa, H. Yanagihara, K. Uwabo, E. Kita, and K. Mibu, Composition shift as a function of thickness in  $\text{Fe}_{3-\delta}\text{O}_4$  (001) epitaxial films, *Jpn. J. Appl. Phys.* **49**, 080216 (2010).
- [61] J. Okabayashi, S. Miyasaka, K. Hemmi, K. Tanaka, S. Tajima, H. Wadati, A. Tanaka, Y. Takagi, and T. Yokoyama, Investigating orbital magnetic moments in spinel-type  $\text{MnV}_2\text{O}_4$  using X-ray magnetic circular dichroism, *J. Phys. Soc. Jpn.* **84**, 104703 (2015).
- [62] J. Okabayashi, S. Miyasaka, M. Takahashi, and S. Tajima, Local electronic and magnetic properties of ferro-orbital-ordered  $\text{FeV}_2\text{O}_4$ , *Jpn. J. Appl. Phys.* **57**, 0902BD (2018).
- [63] J. Okabayashi, S. Li, S. Sakai, Y. Kobayashi, T. Mitsui, K. Tanaka, Y. Miura, and S. Mitani, Perpendicular magnetic anisotropy at the Fe/Au(111) interface studied by Mössbauer, x-ray absorption, and photoemission spectroscopies, *Phys. Rev. B* **103**, 104435 (2021).
- [64] X. Chen, X. Zhang, M.-G. Han, L. Zhang, Y. Zhu, X. Xu, and X. Hong, Magnetotransport anomaly in room-temperature ferrimagnetic  $\text{NiCo}_2\text{O}_4$  thin films, *Adv. Mater. (Weinheim)* **31**, 1805260 (2019).
- [65] H. Koizumi, I. Suzuki, D. Kan, J.-I. Inoue, Y. Wakabayashi, Y. Shimakawa, and H. Yanagihara, Spin reorientation in tetragonally distorted spinel oxide  $\text{NiCo}_2\text{O}_4$  epitaxial films, *Phys. Rev. B* **104**, 014422 (2021).
- [66] D. Kan, M. Mizumaki, M. Kitamura, Y. Kotani, Y. Shen, I. Suzuki, K. Horiba, and Y. Shimakawa, Spin and orbital magnetic moments in perpendicularly magnetized  $\text{Ni}_{1-x}\text{Co}_{2+y}\text{O}_{4-z}$  epitaxial thin films: Effects of site-dependent cation valence states, *Phys. Rev. B* **101**, 224434 (2020).
- [67] J. Okabayashi, Y. Miura, and H. Munekata, Anatomy of interfacial spin-orbit coupling in Co/Pd multilayers using X-ray magnetic circular dichroism and first-principles calculations, *Sci. Rep.* **8**, 8303 (2018).